

Journal of Materials Chemistry C

Materials for optical, magnetic and electronic devices

Accepted Manuscript

This article can be cited before page numbers have been issued, to do this please use: A. Mazzotti, K. Intonti, A. Sessa, L. Viscardi, O. Durante, A. Pelella, S. O'sullivan, V. Patil, P. Hurley, L. Ansari, F. Gity and A. Di Bartolomeo, *J. Mater. Chem. C*, 2026, DOI: 10.1039/D6TC00385K.



This is an Accepted Manuscript, which has been through the Royal Society of Chemistry peer review process and has been accepted for publication.

Accepted Manuscripts are published online shortly after acceptance, before technical editing, formatting and proof reading. Using this free service, authors can make their results available to the community, in citable form, before we publish the edited article. We will replace this Accepted Manuscript with the edited and formatted Advance Article as soon as it is available.

You can find more information about Accepted Manuscripts in the [Information for Authors](#).

Please note that technical editing may introduce minor changes to the text and/or graphics, which may alter content. The journal's standard [Terms & Conditions](#) and the [Ethical guidelines](#) still apply. In no event shall the Royal Society of Chemistry be held responsible for any errors or omissions in this Accepted Manuscript or any consequences arising from the use of any information it contains.

Defect-tuned conduction in ultrathin MoTe₂ field-effect transistors

View Article Online
DOI: 10.1039/D6TC00385K

Adolfo Mazzotti¹, Kimberly Intonti¹, Andrea Sessa¹, Loredana Viscardi², Ofelia Durante¹, Aniello Pelella¹, Stephen O'Sullivan², Vilas Patil², Paul K. Hurley^{2,3}, Lida Ansari², Farzan Gity², and Antonio Di Bartolomeo^{1,}*

¹ Department of Physics "E. R. Caianiello", University of Salerno, via Giovanni Paolo II, Fisciano, Salerno, 84084, Italy.

² Tyndall National Institute, University College Cork, Lee Maltings, Dyke Parade, Cork, T12 R5CP, Ireland

³ School of Chemistry, University College Cork, Cork, Ireland

*Corresponding author e-mail address: adibartolomeo@unisa.it

Abstract

In atomically thin electronics, interfaces and interfacial defects play a critical role in determining device performance. Herein, the interfaces with metal contacts, gate dielectric, and ambient environment are systematically investigated in p-type field-effect transistors with an ultrathin MoTe₂ channel, through temperature- and pressure-dependent measurements, supported by density functional theory calculations. The device performance, likely influenced by Te and Mo vacancies, is enhanced under reduced pressure. Low and nearly symmetric Schottky barrier heights around (37 ± 3) meV are extracted at the metal/semiconductor interfaces through temperature-dependent measurements. The temperature dependence of the mobility suggests that ionized-impurity scattering



possibly associated with Te and Mo vacancies, as a relevant transport mechanism below 300 K, while acoustic-phonon scattering prevails at higher temperatures. Both the subthreshold swing and threshold voltage increase exponentially with temperature, consistent with thermally activated transport mechanisms from band-tail states. A stepwise increase in pressure, starting from vacuum and gradually introducing ambient air, leads to reduced mobility and conductance, which is consistent with progressive molecular physisorption that introduces additional scattering. Near atmospheric pressure, adsorbates are likely to contribute significantly to p-type doping. Taken together, these results elucidate how vacancies, interface traps, and surface adsorbates may govern charge transport in MoTe₂ and provide quantitative guidelines for defect and interface engineering that may also be relevant to other two-dimensional semiconductor devices.

Keywords: 2D materials, MoTe₂, interfaces, defects, temperature, pressure, transistor

1. Introduction

Two-dimensional materials have attracted increasing attention in recent years since they exhibit properties that are not accessible in conventional three-dimensional crystals¹⁻³. As traditional semiconductors approach their scaling limits, low-dimensional semiconductors offer one of the most promising routes to further downscale electronic devices. Significant progress has been made along this direction, and many two-dimensional semiconductors, such as transition metal dichalcogenides (TMDs), have been integrated into high-performance field-effect transistors (FETs)⁴⁻⁹. They have been widely employed in the development of logic circuits for digital electronics, providing a viable alternative to standard CMOS technology¹⁰⁻¹⁴. Beyond digital logic, 2D materials have enabled a broad range of device concepts, including photodetectors¹⁵⁻¹⁷, gas sensors^{18,19}, and neuromorphic devices²⁰⁻²⁴. More advanced fabrication and integration strategies have further enabled multifunctional devices based on 2D layered materials, combining memory and computing capabilities and supporting functions such as logic-gate operations, edge-oriented computing, and brain-inspired behaviors including adaptive learning²⁵.



Practical device performance is tightly linked to how the 2D material is produced and integrated. Scalable growth routes often yield polycrystalline films where grain boundaries and related defects can dominate carrier scattering and recombination, whereas alternative processing routes emphasize interface cleanliness and film quality for robust operation²⁶. A central challenge across 2D electronics is therefore stability and defect control. In TMDCs, point defects, impurities, dislocations, and grain boundaries can introduce mid-gap states that act as trap/detrapping and recombination centers, affecting mobility, subthreshold swing, hysteresis, and time-dependent response^{27,28}.

Molybdenum ditelluride (MoTe_2) is a compound belonging to the family of TMDs and can be found in both a semiconducting (2H) phase, or in a semi-metallic (1T') phase with a slight band overlap close to the Fermi level²⁹. 2H- MoTe_2 has a hexagonal structure and possesses a narrow indirect bandgap of 0.9 eV in the bulk form and a direct bandgap of 1.1 eV in the few-layer form³⁰. In the 1T'- MoTe_2 atoms are arranged in a monoclinic structure with in-plane anisotropy, which makes it ideal for applications like polarized photodetectors^{31,32}. MoTe_2 requires a minimum amount of energy to undergo a transition from 2H to 1T', 0.035 eV compared to 0.8 eV in the case of MoS_2 ^{33,34}. The transition can be achieved with various techniques, such as strain³⁵, temperature³⁶ or laser pulses³⁷.

This phase versatility brings to the forefront one of the main technological challenges in 2D electronics, namely the formation of low-resistance electrical contacts. Large-area MoTe_2 FET arrays have been realized by chemically assembling vertical 1T'/2H MoTe_2 heterophase structures, where metallic 1T'- MoTe_2 acts as the contact and semiconducting 2H- MoTe_2 as the channel. This vertical van der Waals contact geometry enables ohmic behavior with strongly reduced contact resistance and field-effect mobilities comparable to exfoliated single-crystal MoTe_2 , underscoring the suitability of this material for scalable and low-resistance electronic devices³⁸.



Due to its relatively small bandgap, MoTe₂ can support concurrent electron and hole transport, making it attractive for both electronic and optoelectronic devices. However, this same ambipolar potential is often accompanied by reliability issues, widely linked to Te vacancies and other defect species. Recent work has demonstrated that targeted chemical treatments can “heal” Te vacancies and systematically shift threshold voltage and polarity, providing direct evidence that defect engineering is an effective route to improve reproducibility and control in MoTe₂ FETs³⁹.

Beyond contact engineering, the overall performance of MoTe₂-based FETs is further governed by the transport properties of the semiconducting channel itself, which can display ambipolar behaviour depending on a variety of intrinsic and extrinsic factors^{40–42}. These include interactions with atmospheric molecules, charge trapping and defects at the oxide interface, as well as intrinsic crystalline point defects within the MoTe₂ lattice. Density Functional Theory (DFT) and Kelvin Probe Force Microscopy (KPFM) prove that physisorbed oxygen molecules on the MoTe₂ surface can increase its work function toward p-type behaviour⁴³. On the contrary, it has been demonstrated that the formation of tellurium vacancies or tellurium adatoms can induce a pronounced n-type conduction⁴⁴.

While sensitivity to defects and environmental factors enables ambipolar transport, it also highlights the need for strategies that allow a more deterministic and controllable modulation of the carrier type. Carrier modulation in ambipolar few-layer MoTe₂ FETs has been achieved by employing MgO surface charge transfer doping. The doping process allows for reversible switching of the carrier polarity from p-type to n-type by adjusting the thickness of the MgO layer and the number of MoTe₂ layers. Notably, electron mobility in MoTe₂ transistors is significantly enhanced, from 0.1 to 20 cm²/V·s, after doping with 37 nm of MgO. This carrier modulation enables high-performance complementary inverters with a high DC gain (>25) and photodetectors, making it a promising approach for the development of advanced electronic and optoelectronic devices based on MoTe₂⁴⁵.



However, achieving reliable carrier modulation alone is not sufficient if long-term stability and reproducibility are compromised by environmental degradation. Air-stable monolayer MoTe₂ FETs have been demonstrated by encapsulating MoTe₂ in hBN and employing a multigate architecture that electrostatically dopes the contacts, enabling low and tunable contact resistance for both electrons and holes. This device concept allows independent control of threshold voltage and contact resistance and has been exploited to realize a complementary inverter and electrostatically defined p-i-n diodes on a single MoTe₂ flake, highlighting the suitability of monolayer MoTe₂ for integrated logic and optoelectronic circuits⁴⁶.

In this context, despite the significant progress in MoTe₂-based electronics, optimizing device performance still requires a deeper understanding of its behavior at the atomic scale. In two-dimensional materials, interfaces are of paramount importance, since the reduced thickness enhances the influence of surface and interfacial phenomena. These effects can critically determine the electrical properties of MoTe₂-based devices.

This work investigates electrical transport in back-gated MoTe₂ field-effect transistors by combining controlled pressure and temperature experiments. Device characteristics are tracked while pumping down from ambient conditions to high vacuum, and the evolution of the FET figures of merit is discussed together with the role of metal/MoTe₂ contacts. Temperature-dependent measurements are subsequently carried out to extract contact-related parameters and to analyze how conduction, subthreshold swing, and threshold voltage evolve with temperature. Vacuum annealing is employed to probe defects dynamics and their impact on the electrical response. Finally, measurements conducted while progressively increasing the pressure from vacuum are used to assess how surface exposure affects transport through adsorption processes. Each of the mechanisms proposed on the basis of experimental results, is supported by DFT simulations. Unlike previous studies^{47,48}, here we perform systematic temperature and pressure sweeps to shed light on the different phenomena governing electrical transport in the material. These results, combining experimental measurements



and DFT-based simulations, provide a consistent framework to disentangle the contribution of contacts, traps, and surface adsorbates in MoTe₂-based devices.

2. Material and methods

Figure 1-a shows the hexagonal crystalline structure of a monolayer 2H-MoTe₂ from both top and side view. The structure consists of an atomic layer of molybdenum atoms (blue) located between two layers of tellurium atoms (purple). The MoTe₂ flake was used as the channel of a FET, fabricated as described in the following. Flakes of 2H-MoTe₂ are mechanically exfoliated and transferred over a substrate of highly p-doped silicon wafer, which serves as the gate of the FET. The gate dielectric consists in a layer of 85 nm silicon dioxide (SiO₂) thermally grown on the p-Si. After the flake transfer, Ni/Au (20 nm/150 nm) metallic contacts are formed by photolithography, electron-beam metal evaporation, followed by the standard lift-off process. A three-dimensional schematic of the final device is reported in Figure 1-b. The two metallic contacts on top of the MoTe₂ flake are used as the drain and the source of the transistor, while the gate voltage is applied to the p-Si substrate. The optical top-view image of the device is shown in Figure 1-c. The active area of the MoTe₂ flake, corresponding to about 15.5 μm², is highlighted in light blue. The channel length and width, i.e. the average linear dimensions of the active area, correspond to L = 2.23 μm and W = 6.95 μm, respectively. Figure 1-d shows the Raman spectrum of the 2H-MoTe₂ flake, acquired using a Horiba XploRA plus Raman microscope with an EMCCD detector and a 532 nm laser excitation. Three main peaks are evident at 170 cm⁻¹, 230 cm⁻¹ and 288 cm⁻¹, which correspond to the A_g¹, E_{2g}¹ and B_{2g}¹ vibrational mode respectively⁴⁹⁻⁵¹. These modes consist of vibrations of tellurium and molybdenum atoms, as illustrated in Figure 1-d. The B_{2g}¹ peak is absent in monolayers and in bulk MoTe₂, but becomes Raman-active in few-layer flakes due to the breaking of translational symmetry⁵². Specifically, its intensity is reported to be maximal for bilayers and to decrease with increasing thickness⁵³. A minor peak is also detected at 139 cm⁻¹, which can be attributed to a second-order Raman process, as observed in other dichalcogenides^{54,55}. The intensity ratio between B_{2g}¹ and E_{2g}¹



peaks is ~ 1.5 , while frequency separation between these two modes is $\sim 61 \text{ cm}^{-1}$, indicating a few layers (approximately 3-5 layers) MoTe₂ flake⁴⁹⁻⁵¹.

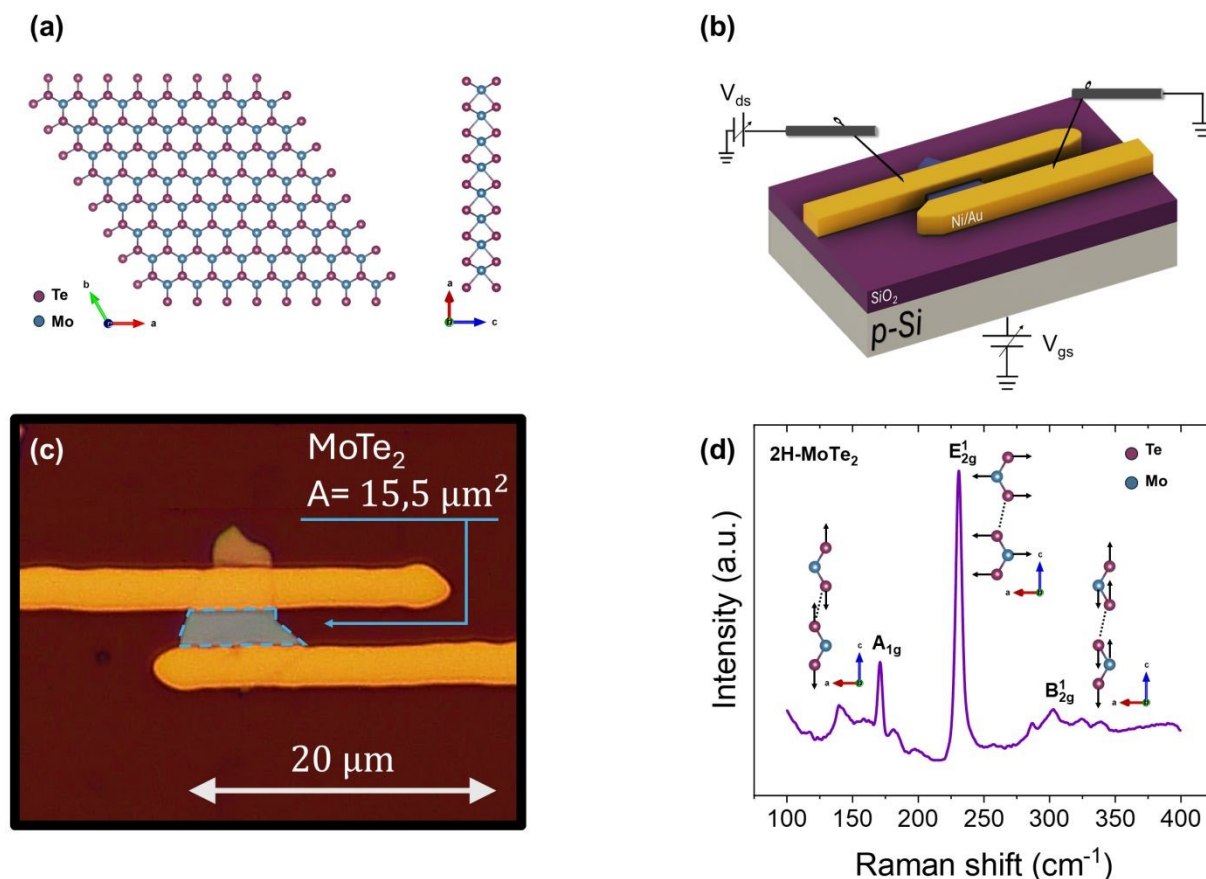


Figure 1 . **Device structure and morphology.** Crystalline structure of a monolayer 2H-MoTe₂ from different perspectives (a). Three-dimensional schematic of the device (b). Optical image of the device, the dashed line highlights the active area of the MoTe₂ flake (c). Raman spectrum of the 2H-MoTe₂ flake on Si/SiO₂ substrate (d).

The electrical measurement of the system is conducted using a Keithley semiconductor characterization system 4200-SCS in combination with a Lakeshore TTPX cryogenic probe station. The station is equipped with a rotative pump and a turbomolecular pump, which enable two different vacuum levels inside the probe chamber. The reported electrical characterization refers to a single representative device; however, multiple devices were fabricated within the same batch and measured under the same experimental protocol. Consistent behaviour and reproducible results were observed across all measured devices.



The band structure calculations were performed within the framework of Density Functional Theory (DFT), employing a linear combination of numerical atomic orbital (LCAO) basis sets as implemented in QuantumATK⁵⁶. Norm-conserving pseudopotentials from the PseudoDojo library were used in combination with medium-quality basis sets⁵⁷. Brillouin zone integration was carried out using the Monkhorst-Pack k -point sampling scheme⁵⁸, with a density of approximately 10 k -points per \AA^{-3} . A real-space grid energy cutoff of 115 Hartree was applied.

Structural optimizations were conducted using the Perdew-Burke-Ernzerhof (PBE) exchange-correlation functional within the generalized gradient approximation (GGA), while van der Waals (vdW) interactions were accounted for via the Grimme DFT-D3 dispersion correction method⁵⁹. Although GGA is known to underestimate band gaps compared to hybrid functionals such as HSE^{60,61}, this limitation does not affect the conclusions, as all calculations employed the same functional consistently. All geometries were relaxed using the Limited-memory Broyden-Fletcher-Goldfarb-Shanno (L-BFGS) algorithm until the maximum force on any atom was less than 0.02 eV/ \AA .

To study the impact of physisorbed oxygen molecules, a slab model of 2H-MoTe₂ was constructed using equilibrium lattice parameters of $a = 3.52 \text{ \AA}$ and $c = 13.96 \text{ \AA}$, representing the hexagonal phase^{61,62}. Both bulk and thin-film systems were considered, including structures with molybdenum (Mo) and tellurium (Te) vacancies to investigate their effects on electronic properties. To analyse the effects of the oxygen adsorbate on MoTe₂ surface, a single oxygen molecule on a 5 x 5 x 1 three-layer MoTe₂ supercell, corresponding to the density of $\approx 4 \times 10^{13} \text{ cm}^{-2}$, has been considered.

To prevent the emergence of artificial electric fields due to the asymmetry introduced by the O₂ molecule adsorbed on one side of the slab, Neumann and Dirichlet boundary conditions were applied to the O₂-covered and bare surfaces, respectively. This approach provides an alternative to standard dipole correction methods in slab-based simulations⁶³.



3. Results and discussion

The electrical characterization was conducted at room temperature and in the dark. Figure 2-a shows the IV curve, on a semi-logarithmic scale, for three different pressures: 1 bar, 10 mbar, and 10^{-3} mbar (violet, blue, and green curves respectively), and with a grounded gate. Regardless of the pressure, the current does not increase linearly with the applied voltage, either positive or negative, as shown in the inset, which displays the IV curve under 1 bar pressure in a linear scale. Such behaviour is typical of a metal-semiconductor interface with a Schottky barrier. In the present case, nickel contacts have work function $\Phi_M \approx 5.0$ eV whereas the 2H-MoTe₂ work function Φ_S can be higher than 5.6 eV⁶⁴, and a Schottky barrier for holes can originate after Fermi level alignment, being $\Phi_M < \Phi_S$ ^{65,66}. For the device under study, measured in a standard two-probe configuration, each contact likely forms a Schottky junction and hence a potential barrier for hole injection. Therefore, the system can be modeled by two back-to-back Schottky diodes: when a certain voltage is applied, one junction is forward-biased while the other is reverse-biased^{67,68}. In such a configuration, the measured current is predominantly governed by the reverse-biased junction, so each branch of the IV curve effectively reflects reverse conduction, at both positive and negative biases. Nevertheless, the barrier height depends on the applied bias voltage, for instance, through image force lowering, so the current does not saturate at either positive or negative bias. Within the thermionic emission model, each branch of the IV curve can be fitted using the equation⁶⁹:

$$I_d = I_0 \exp\left(\frac{qV}{nK_B T}\right) \left[1 - \exp\left(-\frac{qV}{K_B T}\right)\right] \quad (1)$$

$$I_0 = AA^* T^2 \exp\left(-\frac{\Phi_B}{K_B T}\right) \quad (2)$$

where I_0 is the reverse saturation current, q is the elementary charge, n is the ideality factor of the junction, K_B the Boltzmann constant and T the absolute temperature, Φ_B is the voltage dependent Schottky barrier height, A is the contact area, and A^* the so-called Richardson constant. The results of the fit (red and orange solid lines) are reported in the inset of Figure 2-a. Moreover, the increase in



current observed under vacuum conditions can be attributed to a reduction of the hole Schottky barrier at the contacts^{70,71}, and possibly to a decrease in the channel scattering rate. These effects outweigh the reduction in conductivity resulting from the lower p-doping level caused by the desorption of adsorbed molecules in vacuum.

The current flowing within the channel can be modulated by the gate voltage V_{gs} , as shown in Figure 2-b, which shows the transfer characteristics at a drain bias of $V_{ds} = 500$ mV, measured in air (1 bar) and under vacuum (10 mbar and 10^{-3} mbar). The gate current I_g was monitored throughout the measurements and remained below 10^{-10} A over the relevant bias range. Therefore, the recorded transfer characteristics are not affected by gate leakage. Independent of the pressure, the material shows a p-type behaviour, as evidenced by the increase in current under increasingly negative gate bias. This behaviour is consistent with p-type doping expected from Te and, predominantly, Mo vacancies, which are predicted to contribute to the hole concentration based on DFT calculations (Figure 2-c,d). Indeed, the simulation shows that these vacancies shift the Fermi level toward lower energies, rendering the crystal p-type, while simultaneously introducing defect states within the bandgap. The transistor current arises from the modulation of hole concentration in the channel, which is lowered at negative gate biases. The gate voltage sweeping direction strongly affects the current, resulting in a pronounced hysteresis. This behaviour is common in 2D materials and is strongly influenced by the molecules adsorbed on the channel's surface and by defects within the material^{72,73}. The holes field effect mobility can be computed according to the equation:

$$\mu_p = \frac{L}{WV_{ds}C_{ox}} \left| \frac{dI_{ds}}{dV_{gs}} \right| \quad (3)$$

where L and W are the channel dimensions previously defined, $C_{ox} = 4.06 \times 10^{-8}$ F/cm² is the oxide capacitance, and the derivative of the drain current with respect to the gate voltage is computed in the linear region of the positive branch of the transfer curve (negative to positive voltage sweep) through a linear fit. The threshold voltage, V_{th} , is then determined by linear extrapolation of the fitted transfer



curve. The same procedure is applied to all transfer curves in this work; however, the linear fitting region depends on the measurement conditions. Therefore, the V_{gs} fitting window is selected case by case, as a fixed window would not be suitable^{74–76}. At ambient pressure, the drain current varies between about 0.12 μA (at $V_{gs} = +30\text{V}$) and 0.75 μA (at $V_{gs} = -30\text{V}$), hence the I_{ON}/I_{OFF} ratio is 6.47 under these conditions. Hysteresis can be quantified by its maximum width H_w , which is equal to 32 V at ambient temperature and pressure. Under the same conditions, the hole mobility is $\mu_p = 0.26 \text{ cm}^2\text{V}^{-1}\text{s}^{-1}$, while the threshold voltage is $V_{th} = 29.62 \text{ V}$. The low mobility is consistent with the presence of intrinsic defects in the material, such as Te or Mo. Moreover, since the electrical characterization is performed in a two-probe configuration, the extracted field-effect mobility includes the contribution of the contact resistance R_c , which adds in series to the channel sheet resistance R_{sh} ⁷⁷. As a result, the absolute mobility values can be underestimated when the transport is partially contact-limited. Nevertheless, all measurements were carried out using the same device geometry and the same protocol while varying pressure and temperature; therefore, the reported pressure/temperature trends remain meaningful and are corroborated by consistent variations in other parameters. Figure 3-e reports the effect of pressure on μ_p (blue) and V_{th} (red). In agreement with the previous observations, current is larger and shows minor fluctuations in vacuum, possibly due to the decrease in SBH and in scattering rate. This could determine a higher mobility (up to $1.03 \text{ cm}^2\text{V}^{-1}\text{s}^{-1}$ at $P = 10^{-3} \text{ mbar}$), corresponding to a steeper curve, at lower pressure. The reduction of adsorbed air molecules determines a left-shift of the threshold voltage to 10.52 V. This behavior will be analyzed in detail later in the discussion. The effect of pressure on I_{ON}/I_{OFF} and H_w is made clear in Figure 2-f. The I_{ON}/I_{OFF} ratio increases up to 9.81, while the hysteresis width decreases in vacuum, indicating that part of the hysteresis is related to surface-adsorbed molecules. Under vacuum, the reduced adsorbate coverage typically mitigates these surface-related traps, leading to a narrower hysteresis. However, the two branches of the curve remain separated, with $H_w = 16.25 \text{ V}$ at $P = 10^{-3} \text{ mbar}$, suggesting that additional trapping centers are still active. To check the device-to-device variability, more than 10 similar devices were examined under comparable measurement conditions, namely



under vacuum (10^{-3} mbar), in the dark, and at room temperature. Across this set of devices, the extracted field-effect mobility was found to range from $0.59 \text{ cm}^2 \text{ V}^{-1} \text{ s}^{-1}$ up to $2.25 \text{ cm}^2 \text{ V}^{-1} \text{ s}^{-1}$, the hysteresis width from 17 V to 24 V, and the $I_{\text{ON}}/I_{\text{OFF}}$ ratio between 6 and 9. In addition, the current levels were found to be nearly the same across the investigated devices, with a maximum current of about $3.3 \mu\text{A}$ reached at $V_{\text{gs}} = -30 \text{ V}$ and $V_{\text{ds}} = +0.5 \text{ V}$. Moreover, we highlight that the overall trends of the IV characteristics remain consistent with those discussed throughout the manuscript, providing further support for the interpretation of the transport behavior of MoTe_2 transistors.

This residual hysteresis is consistent with intrinsic trap states at the channel/dielectric interface and defect-related states within MoTe_2 , which are not affected by desorption. An estimate of this trap population can be obtained from the hysteresis width, which is related to the net trapped charge and the corresponding effective trap density n_t as^{78,79}:

$$n_t = \frac{\Delta Q_t}{q} = \frac{C_{ox} H_W}{q} \quad (4)$$

where C_{ox} is the gate-oxide capacitance per unit area and H_W is the hysteresis width defined above, and q is the elementary charge. Using this relation, an effective trap density of $n_t \sim 10^{12} \text{ cm}^{-2}$ is estimated at $P = 10^{-3}$ mbar.



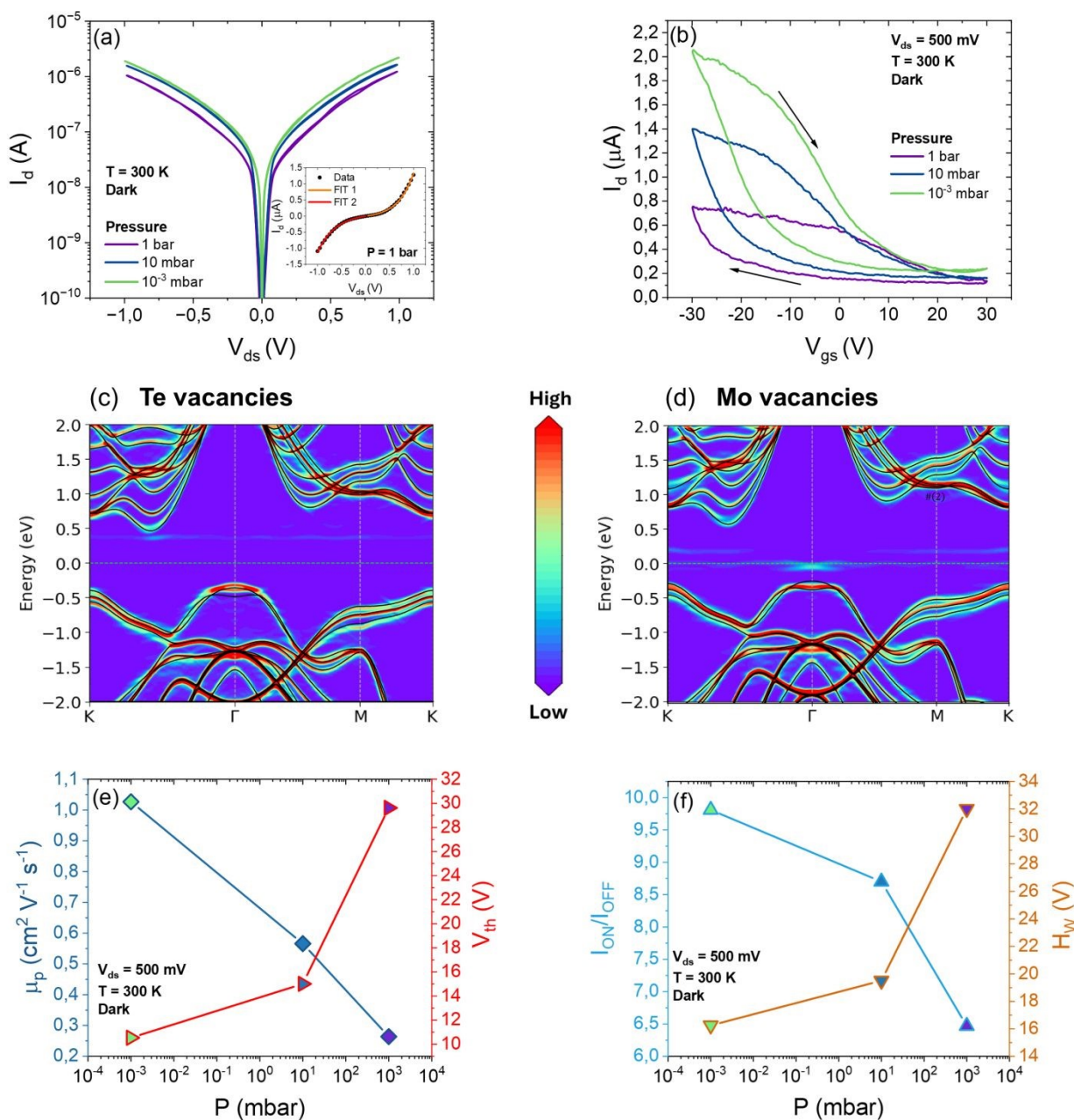


Figure 2 **Electrical characterization at different pressures.** IV curves on a semi-logarithmic scale measured at three different pressures and with grounded gate; the inset shows the 1 bar IV curve on a linear scale with an exponential fit for each branch (a). Transfer characteristics on a linear scale for $V_{ds} = 500$ mV and different pressures (b). Unfolded band structure of the MoTe₂ film with Te (c) and Mo (d) vacancies, shown as contour plots of the total spectral weight intensity. The primitive-cell band structure of pristine MoTe₂ is overlaid as black solid lines. The localized states associated with Te and Mo vacancies appear close to the conduction band edge (Te vacancy) and the valence band edge (Mo vacancy). The zero of energy corresponds to the Fermi level. Field effect mobility (blue y-axis) and threshold voltage (red y-axis) extracted from the transfer curves (e). I_{ON}/I_{OFF} ratio (light blue y-axis) and hysteresis width (brown y-axis) extracted from the transfer curves (f). All measurements in a, b, e, f were conducted in the dark and at room temperature.



Table 1 benchmarks the key figures of merit of the present MoTe₂ FETs against representative reports from the literature^{80–83}. The measured hole mobility is comparable to that reported for similar devices. Concerning the I_{ON}/I_{OFF} ratio, similar values are found in other MoTe₂ devices employing Ni-based contacts under similar dielectric platforms, whereas larger I_{ON}/I_{OFF} ratio is often obtained with different contact schemes, depending on device geometry and measurement conditions.

This comparison suggests that the relatively limited modulation observed in the present work may be influenced by contact injection and trap-related doping. In particular, Ni contacts are expected to favor hole injection in MoTe₂, reducing the effective barrier for holes and increasing the residual conductance in the nominal “OFF” state, which naturally limits the achievable I_{ON}/I_{OFF} . In addition, in-gap trap states and vacancy-related defects can increase the background carrier density and contribute to hysteresis, further raising the off-current and reducing the modulation depth. Consistently, devices measured in vacuum show a reduced hysteresis compared to ambient conditions, supporting the role of adsorbates as an additional, pressure-dependent contribution to the trap landscape.

Several strategies can be adopted to enhance the I_{ON}/I_{OFF} ratio and mobility in these devices. Mainly, improved fabrication protocols and post-fabrication treatments aimed at reducing the density of electrically active defects are expected to strengthen electrostatic channel control^{84,85}. In addition, encapsulation can suppress adsorbate-induced doping and trapping, thereby reducing hysteresis and improving the separation between ON and OFF states^{86,87}. Finally, contact engineering, such as using metallic 1T'-MoTe₂ contact phases, may mitigate contact-limited injection and further increase the achievable modulation⁸⁷.

Nevertheless, the moderate performances as FET do not affect the scope of this work, which focuses on clarifying the role of defects and trap states in charge transport.



Ref.	Contacts	Layer(s)	Dielectric	Environment	$\mu_p \left(\frac{cm^2}{V \cdot s} \right)$	I_{ON}/I_{OFF}	H_W (V)	SBB (meV)
Present work	Ni/Au	3-5	SiO ₂	Vacuum (P=10 ⁻³ mbar)	1.03	9.81	16.25	~37.5
⁸⁰	Ni	multilayer	SiO ₂	Ambient pressure	0.55	~9	~45	150
⁸¹	Ti/Au	multilayer	SiO ₂	Ambient pressure	10 ⁻²	10 ²	-	-
⁸²	Cr/Au	4	SiO ₂	Vacuum (P=10 ⁻² mbar)	-	10 ³	-	-
⁸³	Ti/Au	30	SiO ₂	Ambient pressure	6.4	10 ³	-	120

Table 1 Comparison between present work and representative reports from the literature⁸⁰⁻⁸³.

Figure 3-a shows the output curves in high vacuum (10⁻³ mbar) obtained by stepping the gate voltage from +40 V down to -40V in steps of -10 V. The p-type behavior is confirmed; indeed, a larger current is obtained when a negative gate voltage is applied, independently of the applied bias to the drain. The exponential trend with V_{ds} remains for each value of the gate voltage, with a slight modification of the shape of the curve, which is expected since the gate voltage affects the energetic bands of the material in the channel as well as in the contact region⁶⁵. The modulation of the channel current is affected also by the drain bias as shown by the transfer curves at different V_{ds} , between 0.1V and 1V in Figure 3-b. Being the contact of Schottky type, the current grows exponentially at higher V_{ds} , hence the transfer curves measured at larger drain biases are shifted upward. The effect of the bias on the mobility and threshold voltage is clarified in Figure 3-c. The mobility increases with V_{ds} , reaching a maximum value of 2.70 cm²V⁻¹s⁻¹ for $V_{ds} = 1$ V, which can be attributed to reduced contact resistance and a transition from trap-limited transport to a more delocalized transport regime at higher electric fields. For higher values of V_{ds} , also the threshold voltage is subjected to a slight increase, switching from 7.94 V at $V_{ds} = 0.1$ V up to 13.75 V at $V_{ds} = 1$ V. This behaviour can be explained by the lowering of the effective drain Schottky barrier at higher bias, which requires a more positive gate voltage to fully deplete the channel of holes and turn the transistor off. Finally, Figure 3-d reports the dependence of I_{ON}/I_{OFF} and H_W on V_{ds} . The separation between the ON and OFF states of the transistor is reduced as long as V_{ds} increases. This behaviour can be ascribed to an enhancement of the OFF-state current, due to drain-induced barrier lowering and trap-assisted conduction. The maximum



hysteresis width exhibits a non-monotonic dependence on the drain bias: it initially increases as the bias is raised and subsequently decreases at higher bias values. A possible explanation is the following: at high drain voltages, the stronger lateral electric field enhances charge trapping and detrapping in the dielectric and at the channel interfaces, leading to a widening of the hysteresis. At higher drain bias, however, trap occupancy tends to saturate and diminish the effective threshold shift between the forward and backward sweeps, resulting in a reduced hysteresis width^{79,88–90}.

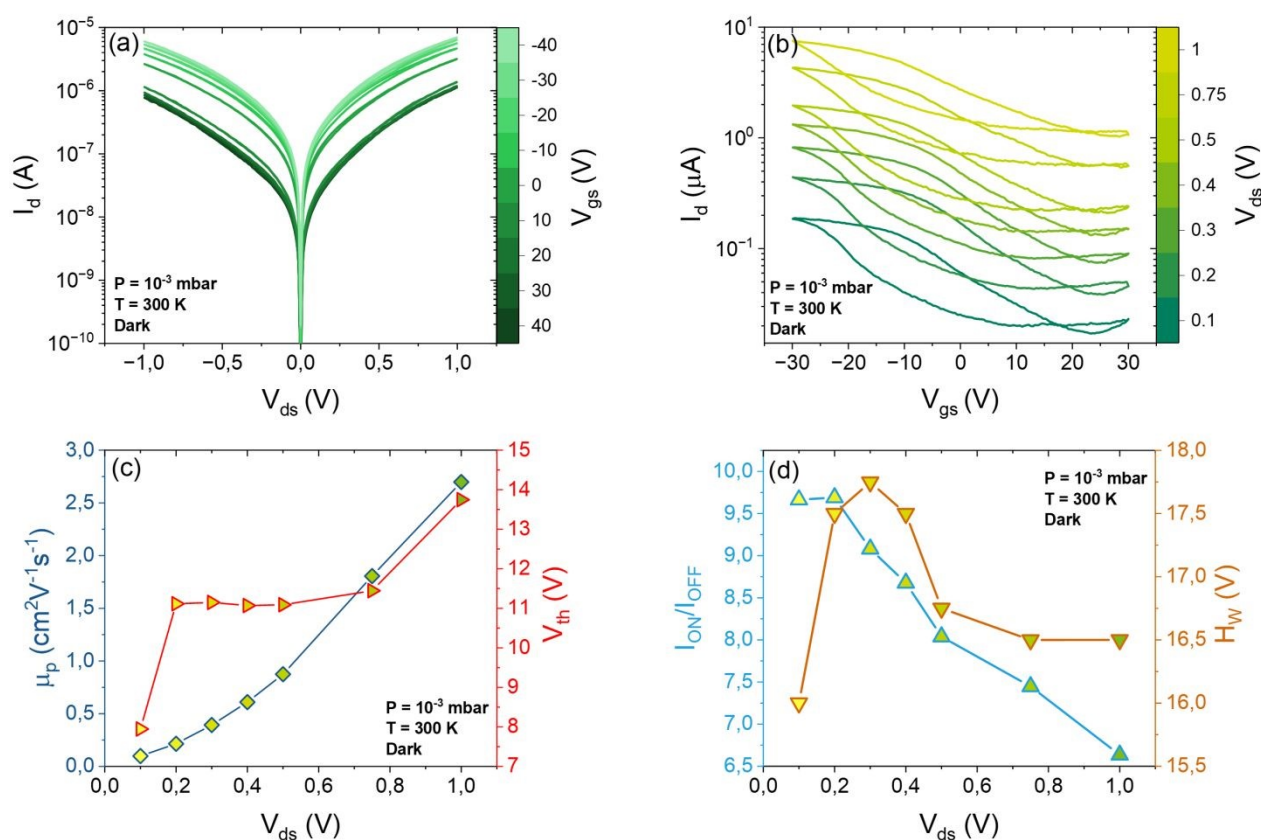


Figure 3 **Electrical characterization in vacuum.** Output characteristics on a semi-logarithmic scale at $P = 10^{-3}$ mbar (a). Transfer characteristics on a semi-logarithmic scale for increasing values of V_{ds} at $P = 10^{-3}$ mbar (b). Field effect mobility (blue y-axis) and threshold voltage (red y-axis) extracted from the transfer curves as a function of the drain bias (c). I_{ON}/I_{OFF} ratio (light blue y-axis) and hysteresis width (brown y-axis) extracted from the transfer curves as a function of the drain bias (d). All measurements were conducted in the dark and at room temperature.

i. Temperature-dependent behavior

Temperature measurements were conducted, in the dark and at $P = 10^{-3}$ mbar, to better understand the transport properties of MoTe_2 . Figure 2-a shows the IV curves at $P = 10^{-3}$ mbar for different



temperatures, increasing from 77 K up to 400 K. At higher temperatures, the increased kinetic energy of charge carriers enhances hole injection at the contacts and the current increases. The plot shows a small asymmetry that gradually diminishes with increasing temperature, consistent with thermionic conduction⁷⁰. Moreover, as the temperature increases, the available thermal energy frees charge carriers from defect traps or localised states within the material. This leads to a higher concentration of mobile carriers and, consequently, a rise in electrical conductance. Such a trend is characteristic of semiconductors, in which electrons in the valence band acquire sufficient energy to be transferred into the conduction band through intragap states, causing the conductivity to grow with increasing temperature⁹¹. The temperature-dependent analysis is useful to extract the Schottky barrier heights (SBHs) at the two metal-semiconductor interfaces. To do this, one can use the temperature dependence of the zero-bias current, I_0 , and construct the Richardson plot, which is typically linear, according to the equation^{70,91}:

$$\ln\left(\frac{I_0}{T^2}\right) = \ln(AA^*) - \frac{\Phi_B}{k_B T} \quad (5)$$

I_0 can be extracted as the intercept of the linear fit of either the forward or reverse bias region of the semi-logarithmic IV curve. The analysis was carried out for both positive and negative values of the drain biases. Figure 4-b reports the Richardson plot computed for $V_{ds} < 0$. The thermionic conduction over the Schottky barrier is confirmed by the linear trend of the Richardson plot, as shown by the linear fit (black dashed line), for temperatures higher than 200 K. At lower temperatures, the deviation from the expected behaviour arises from the onset of conduction mechanisms other than thermionic emission, such as tunnelling or recombination. Moreover, it suggests the presence of spatially inhomogeneous barrier heights and potential fluctuations at the interface, resulting in regions with both low and high barrier heights⁹²⁻⁹⁴. Indeed, according to the model proposed by Werner-Güttler⁹⁵, in the presence of inhomogeneities, the barrier height is treated as a Gaussian distribution with mean value $q\phi_B^0$ and standard deviation σ . At low temperature, charge transport is dominated by preferential conduction through regions with locally reduced barrier height, so the extracted effective



barrier $q\phi_B^{eff}$ deviates from the mean value and the Richardson analysis no longer yields a single temperature-independent barrier. As temperature increases, carriers gain sufficient thermal energy to sample a larger portion of the distribution, and $q\phi_B^{eff}$ approaches the mean barrier $q\phi_B^0$. Therefore, the SBH extracted from the high-temperature linear regime ($T \geq 200$ K), is reliable as an effective/mean barrier representative of the room-temperature interface under the considered bias polarity. The SBHs, extracted as the slopes of the linear fits, are only slightly different with $\Phi_B^{V_d > 0} = (38 \pm 6)$ meV and $\Phi_B^{V_d < 0} = (37 \pm 3)$ meV. The low and similar Schottky barriers at the two contacts are expected, given the relatively high channel current and almost symmetric IV curves. This value is smaller than what would be expected from a simple comparison of Φ_M and Φ_S , indicating that the contact does not follow the ideal Schottky-Mott limit. Instead, the measured barrier suggests that the Ni Fermi level is effectively close to the MoTe₂ valence-band edge at the interface. Such a reduced effective barrier can arise from interface dipoles and charge transfer, the presence of interfacial (gap) states, and the resulting Fermi-level pinning, which strongly modifies the local band alignment compared to the vacuum-level estimate^{96–99}. Moreover, the presence of interface states and defects can lead to Fermi-level pinning, strongly reducing the sensitivity of the barrier height to the metal work function and yielding much smaller effective barriers than those expected from the Schottky-Mott estimate^{100–102}. Finally, considering the presence of barrier inhomogeneity and potential fluctuations, current preferentially flows through locally low-barrier patches, which can further reduce the apparent barrier height compared to a uniform-barrier picture^{70,95}.

Figure 4-c reports the transfer curves at $V_{ds} = 500$ mV for temperatures from 77 K up to 400 K. Consistently with the IV curves, current increases with temperature. Specifically, the trap and localized states, which are progressively emptied as temperature increases due to thermal activation, are more populated when a positive gate bias is applied. Therefore, the temperature-induced increase in current is particularly pronounced when the transistor is in the OFF state. As a result, the OFF-



state current rises with temperature, leading to a corresponding reduction in I_{ON}/I_{OFF} ratio. The p-type behaviour is preserved for each value of temperature in the considered range.

The temperature dependence of the hole field-effect mobility is reported in the double-logarithmic plot in Figure 4-d. μ_p exhibits a power-law increase with temperature from 77 K to 300 K, after which it transitions to a power-law decay. This behaviour can be attributed to distinct scattering mechanisms. At low temperatures, charge transport is mainly limited by scattering from ionized impurities in the material; in this regime, the mobility scales with temperature as $\mu_p \propto T^{\frac{3}{2}}$; on the contrary, mobility decreases like $\mu_p \propto T^{-\frac{3}{2}}$ at higher temperatures because of acoustic phonon scattering which becomes the dominant mechanism. From a linear fit in the double-logarithmic plot the exponents can be extracted, obtaining $\mu_p \propto T^{(1.9 \pm 0.05)}$ for $T < 300$ K and $\mu_p \propto T^{(-2.3 \pm 0.7)}$ for $T > 300$ K. These values are consistent with the two mentioned mechanisms which remain the main ones, however, the slow deviation from theoretical values is to impute to other scattering mechanisms and is consistent with results found in literature^{65,103,104}. The subthreshold swing (SS) was extracted from the transfer as $SS = \left| \frac{d \log I_d}{d V_{gs}} \right|^{-1}$ and its trend as a function of the temperature is reported in Figure 4-e. Typically, one expects the SS to scale linearly with the temperature, according to the equation⁶⁵:

$$SS = \left(\frac{k_B T}{q} \ln 10 \right) \left(1 + \frac{q^2 D_{it}}{C_{ox}} \right) \quad (6)$$

where D_{it} is the density of interface defects and C_{ox} is the oxide capacitance. However, in the case of study, the experimental fit (black dashed lines) demonstrates that the trend is exponential. This can be attributed to band tails, i.e. to defect states near the band edges that decay exponentially into the band gap, resulting in^{105–107}:

$$SS \approx \left(\frac{k_B T}{q} \ln 10 \right) e^{-\frac{E_a}{k_B T}} \quad (7)$$



Where E_a is the activation energy. The equation is valid for $1 \ll \frac{q^2 D_{it}}{C_{ox}}$, which is reasonable considering the device under study. The activation energy extracted from the fit is $E_a = 238$ meV. This value is very close to others found in literature for MoTe_2 and gives the extension of the band tail, that is, of the energy range of defect states above the valence band¹⁰⁸. A similar exponential trend in temperature was observed for the threshold voltage, as visible in Figure 4-f. However, in this case the activation energy, extracted through an exponential fit (black dashed line in figure) is $E_a = 160$ meV. Despite the smaller energy, the exponential behaviour confirms the role of MoTe_2 band tail in the switching behaviour of the transistor.

View Article Online
DOI: 10.1039/C6JM00385K



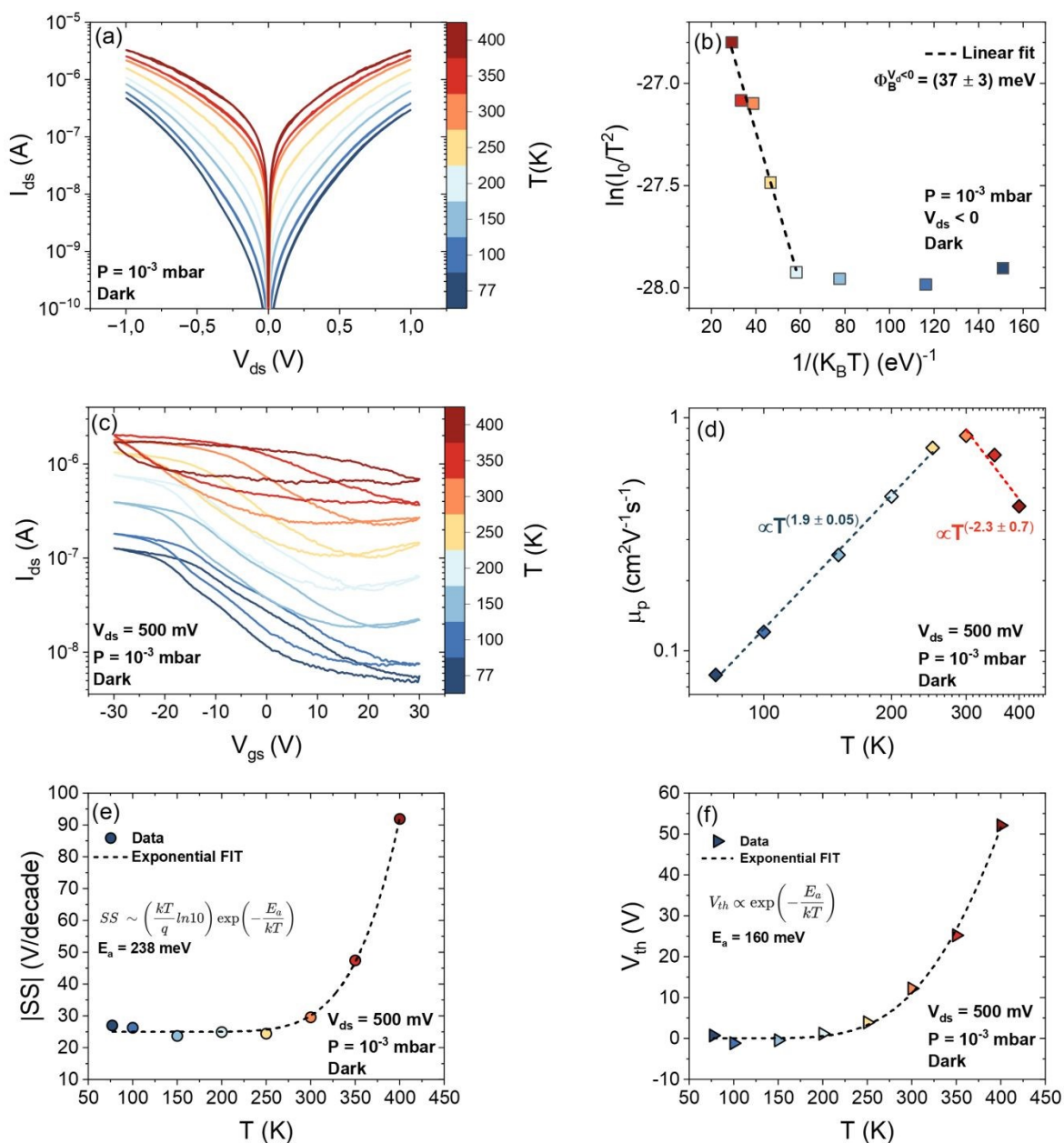


Figure 4 **Electrical characterization as a function of temperature.** IV curves measured at different temperatures from 77 K to 400 K (a). Corresponding Richardson plot for positive drain biases, $V_{ds} > 0$; the black dashed line is a linear FIT (b). Transfer characteristics at $V_{ds} = 500$ mV for temperatures from 77 K to 400 K (c). Field-effect mobility as a function of temperature on a double-logarithmic scale; the blue and red dashed lines indicate linear fits (d). ISSI (e) and V_{th} (f) as a function of temperature with exponential fits (black dashed lines). All measurements were conducted in dark and at $P = 10^{-3}$ mbar.



*i. Defects study*View Article Online
DOI: 10.1039/D6TC00385K

The gate modulation is affected by thermal annealing, as demonstrated in Figure 5-a, which shows the transfer curve at $P = 10^{-3}$ mbar before and after heating the device for 1h at 400 K. It is clear that after the annealing the current is much smaller over the entire V_{gs} range considered, with a reduction of the I_{ON}/I_{OFF} ratio from 9.81 to 3.11. Holes remain the majority charge carriers, even though their mobility is decreased from $\mu_p = 1.03 \text{ cm}^2\text{V}^{-1}\text{s}^{-1}$ to $\mu_p = 0.35 \text{ cm}^2\text{V}^{-1}\text{s}^{-1}$. It is also observed that a slight ambipolar behavior appears after the annealing, with an electron mobility of $\mu_n = 0.06 \text{ cm}^2\text{V}^{-1}\text{s}^{-1}$. This behaviour is consistent with the ambipolar Schottky-barrier transport widely reported in MoTe_2 FETs and likely reflects the strong suppression of p-type conduction (reduced hole density/modified interfacial states), which makes the otherwise weaker electron contribution observable^{41,61,109}. Concurrently, the threshold voltage exhibits a small left shift from 10.0 V to 8.7 V. To properly explain this phenomenon, several observations must be considered. Desorption of surface contaminants can reduce current by diminishing the p-doping effect of O_2 and H_2O molecules, but this is often offset by an increase in current due to a reduction of the hole Schottky barrier at the contacts^{70,71} and decreased adsorbate-induced scattering. The pronounced decrease in current and the suppression of p-type transport after annealing suggest a mechanism beyond desorption. As both Te and Mo vacancies contribute to the p-doping of the material, their passivation suppresses the doping level and contributes to the observed reduction in conductivity. Moreover, a structural phase change is unlikely under the adopted thermal budget, as it is typically induced only by annealing at much higher temperatures ($T > 1000 \text{ K}$)^{110,111}. Finally, oxygen-related processes in MoTe_2 are known to be strongly defect-assisted: vacancies can act as reactive sites that promote oxygen bonding/intercalation, thereby modifying the interfacial potential landscape and the distribution of in-gap states^{112–114}. Therefore, prior to thermal annealing, Mo and Te vacancies could introduce acceptor-like states which capture electrons from the valence band and release holes. At equilibrium this would result in a pronounced p-type behavior. The thermal energy provided during annealing would promote oxidation and passivation of the Te and Mo vacancies, reducing the



concentration of defect-induced holes, consistent with the DFT calculations shown in Figure 5-b. Annealing possibly modifies the distribution of in-gap trap states, as schematically illustrated by the band model in Figure 5-c. In this scenario, before annealing, vacancies increase the hole density (left-side of the image), while as these defects become passivated, the density of the acceptor-like trap states is reduced, leading to a partial suppression of hole conduction and the emergence of weak electron transport (right-side of the image). The observed small shift in the threshold voltage after the annealing can be attributed to the modification of the charges in the trap states⁶⁵.

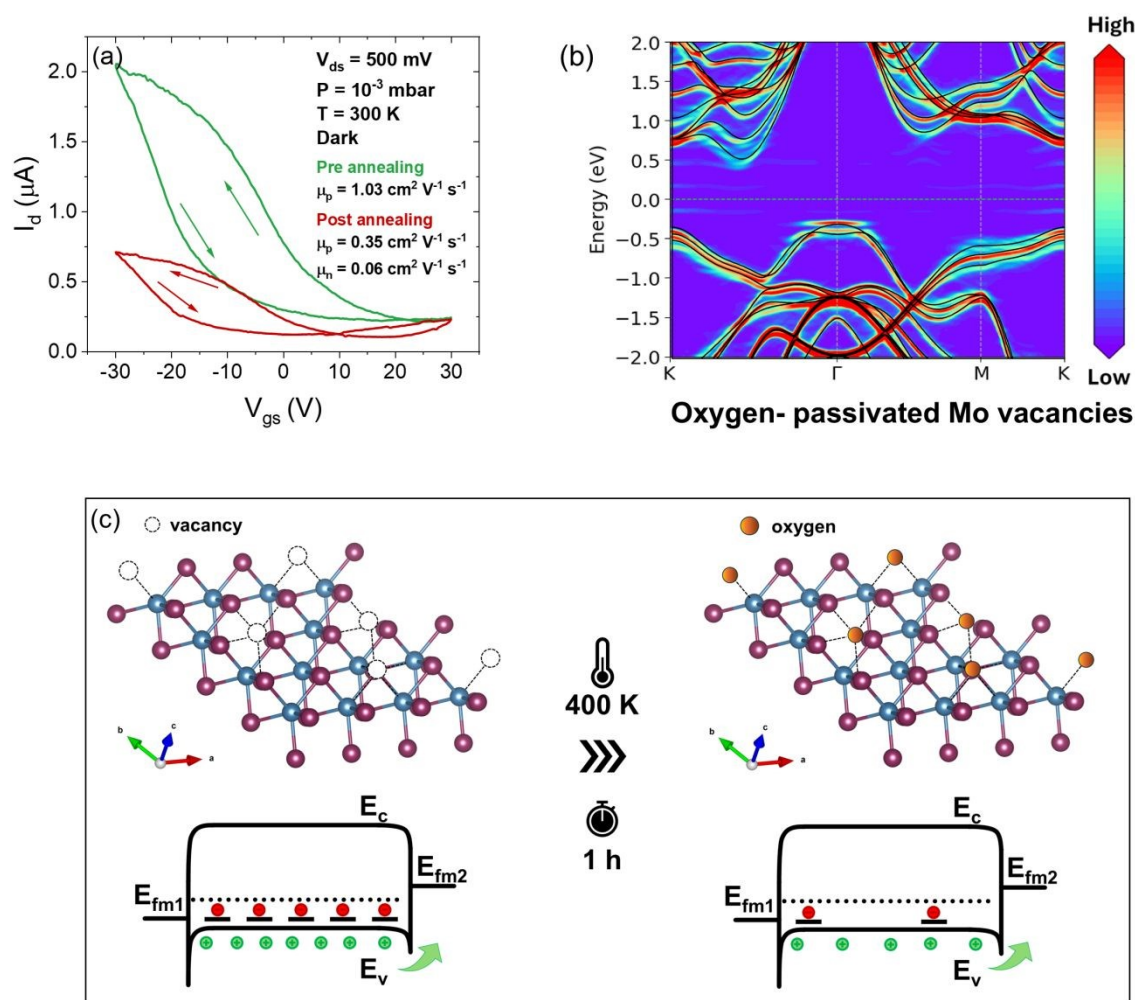


Figure 5 **Electrical characterization as a function of pressure.** Transfer characteristics under dark, at $V_{ds} = 500$ mV, $T = 300$ K and $P = 10^{-3}$ mbar, before (green curve) and after (red curve) thermal annealing at 400 K for 1 h (a). Unfolded band



structure of an oxygen-passivated Mo vacancy in MoTe₂. Oxygen passivation reduces the vacancy-induced p-type doping and associated localized states. Black solid lines represent the primitive-cell band structure of pristine MoTe₂. The zero of energy corresponds to the Fermi level (b). Schematic illustration of the effect of annealing on the device surface and the corresponding band diagram (c).

To further confirm this explanation, the device was studied during the adsorption process, sweeping from 10⁻³ mbar to atmospheric pressure. After a 30 minutes stabilization at each step to allow adsorption, IV and transfer curves were measured. This waiting time was adopted as a conservative criterion; indeed, repeated measurements after each pressure change showed that the device response reached a stable state within this interval. Figure 6-a shows the IV curves obtained for different pressure values during this sweep. The Schottky behavior is maintained independently of pressure, which is expected since it is attributed to the metal/semiconductor interface. At first, the current becomes lower while increasing the concentration of air molecules and then starts to increase, as shown by the conductance plot in Figure 6-b. Specifically, conductance was extracted from the IV curves at small biases, where the current grows linearly with V_{ds}. The initial reduction in conductivity can be explained by the increasing density of scattering centers with pressure. However, to fully understand this non-monotonic trend one must also consider holes mobility. Figure 6-c reports the transfer curves at the different pressures during the sweep. Starting from a post-annealing configuration, with slight ambipolar behavior, the n-type conduction is gradually suppressed due to electronic trapping in adsorbates-induced defect states. The presence of adsorbates on the channel is reflected in noisier curves at higher pressures. The trend of holes mobility is shown in Figure 6-d. μ_p decreases since it linearly depends on the scattering time τ which decreases as the concentration of adsorbates on the channel becomes higher. At first, the conductance $G \propto \mu_p p$ (p is the hole density) follows the trend of μ_p , suggesting that p is not subject to significant variations. When a pressure of 10² mbar is reached, mobility stops decreasing and G starts to increase. From this pressure onwards, the adsorbate related hole concentration possibly becomes dominant, with a consequent p-doping of the channel. The DFT calculations reported in Figures 6-e and f confirm the p-type doping effect of



oxygen physisorption on both pristine MoTe₂ and defective MoTe₂ with an oxygen-passivated Mo vacancy.

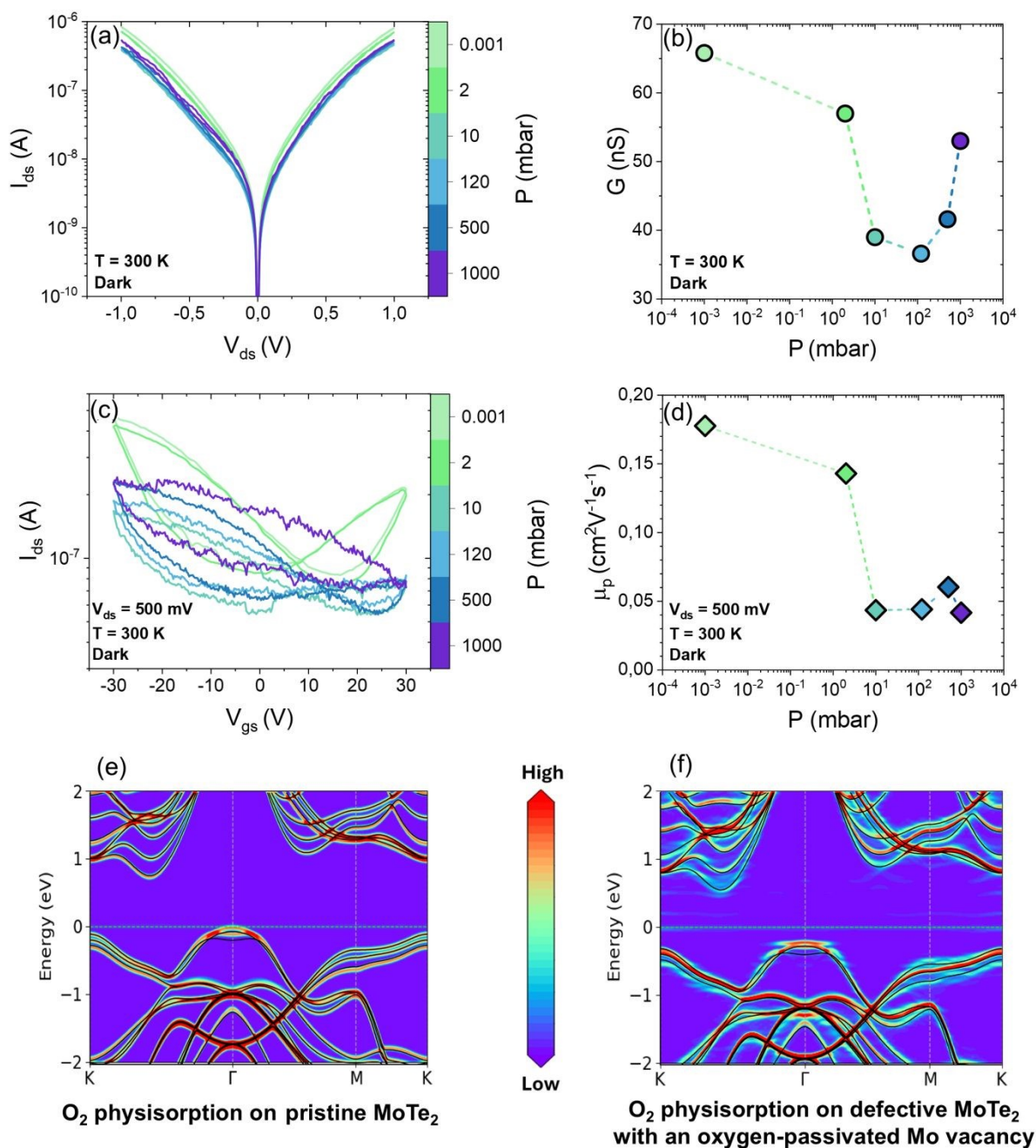


Figure 6 **Electrical characterization as a function of pressure.** IV curves at different pressures, increasing from 10⁻³ mbar up to 1 bar (a). Corresponding conductance as a function of pressure (b). Transfer characteristics at $V_{ds} = 500$ mV for different pressures (c). Pressure dependence of the field-effect mobility (d). Unfolded band structure of O₂ physisorption on the surface of pristine MoTe₂ (e), and defective MoTe₂ with oxygen-passivated Mo vacancy (f). Black solid lines in (e) and (f) denote the primitive-cell band structure of pristine MoTe₂. The zero of energy corresponds to the Fermi level. All measurements a-d were conducted in the dark and at room temperature.



4. Conclusions

View Article Online
DOI: 10.1039/D6TC00385K

This work investigates the electrical behavior of MoTe₂-based field-effect transistors through a combined experimental and theoretical approach. All measurements were performed in the dark using a two-probe configuration. The device exhibits Schottky barriers at the metal/semiconductor interfaces, while the transfer characteristics consistently show p-type behavior, with enhanced conduction under vacuum conditions. Although the studied devices show limited FET performance, this is not a limitation for the present study, which focuses on clarifying the role of defects and trap states in charge transport. Under high vacuum, an increase in mobility with V_{ds} bias is observed, which may be associated with a reduction in contact resistance, accompanied by a reduction in the I_{ON}/I_{OFF} ratio. Temperature-dependent measurements yield nearly symmetric Schottky barrier heights under positive and negative drain bias, $\Phi_B^{V>0} = 38$ meV and $\Phi_B^{V<0} = 37$ meV respectively. Analysis of the temperature dependence of the mobility suggests that ionized-impurity scattering is an important transport mechanism below 300 K, possibly consistent with the presence of unpassivated Te and Mo vacancies. At higher temperatures acoustic-phonon scattering appears to become the prevailing mechanism. Both the SS and the V_{th} increase exponentially with temperature, in agreement with thermally activated transport from band-tail states. Following thermal annealing, a reduction in channel conductance under vacuum is observed, suggesting a possible role of oxygen passivation of vacancies leads to a suppression of p-doping. Finally, increasing measurement chamber pressure enhances molecular adsorption, which is consistent with a reduction in both mobility and conductance through introducing additional scattering processes; however, near atmospheric pressure, the p-doping effect of adsorbates appears to become significant. In summary, this joint experimental and DFT study suggests that distinct classes of defects, such as intrinsic vacancies, interface/border traps, and surface adsorbates, collectively may govern charge transport in MoTe₂ FETs.



Funding Sources

A.D.B. acknowledges the financial support from the University of Salerno, with grant ORSA254881. This work was also supported by Research Ireland (formerly Science Foundation Ireland) through the AMBER Research Centre (SFI-12/RC/2278_P2) and the Frontiers for the Future PI Award (24/FFP-A/13329). Support from the EU MSCA project 101153933 is also acknowledged. The authors acknowledge the SFI/HEA Irish Centre for High-End Computing (ICHEC) for the provision of computational facilities and support. The authors also acknowledge K. Momma and F. Izumi for the software "VESTA 3 for three-dimensional visualization of crystal, volumetric and morphology data," *J. Appl. Crystallogr.*, 44, 1272-1276 (2011).

References

- 1 W. Ren, P. Boggild, J. M. Redwing, K. S. Novoselov, L. Sun, Y. Qi, K. Jia, Z. Liu, O. Burton, J. A. Alexander-Webber, S. Hofmann, Y. Cao, Y. Long, Q.-H. Yang, D. Li, S. H. Choi, K. K. Kim, Y. H. Lee, M. Li, Q. Huang, Y. Gogotsi, N. Clark, A. Carl, R. Gorbachev, T. Olsen, J. Rosen, K. S. Thygesen, Prof. Dr. D. K. Efetov, B. S. Jessen, M. Yankowitz, J. Barrier, R. K. Kumar, F. Koppens, H. Deng, X. Li, S. Dai, D. Basov, X. Wang, S. Das, X. Duan, Z. Yu, M. Borsch, A. C. Ferrari, R. Huber, M. Kira, F. Xia, X. Wang, Z.-S. Wu, X. Feng, P. Simon, H.-M. Cheng, B. Liu, Y. Xie, W. Jin, R. R. Nair, Y. Xu, H.-B. Zhang, V. Pellegrini, B. Qu, M. Lemme, A. Katiyar, J.-H. Ahn, I. Aharonovich, M. C. Hersam, S. Roche, Q. Hua, G. Shen, T.-L. Ren, C. M. Koo, N. A. Koratkar, R. J. Young and A. Pollard, *2D Mater.*, DOI:10.1088/2053-1583/ae2b82.
- 2 A. Di Bartolomeo, *Nanomaterials*, 2020, **10**, 579.
- 3 M. B. Askari, P. Salarizadeh, P. Veisi, E. Samiei, H. Saeidfirozeh, M. T. Turchi Moghadam and A. Di Bartolomeo, *Micromachines*, 2023, **14**, 691.
- 4 V. Patil, J. Kim, K. Agrawal, T. Park, J. Yi, N. Aoki, K. Watanabe, T. Taniguchi and G.-H. Kim, *Nanotechnology*, 2021, **32**, 325603.
- 5 M. W. Iqbal, M. Z. Iqbal, M. F. Khan, M. A. Shehzad, Y. Seo, J. H. Park, C. Hwang and J. Eom, *Sci Rep*, 2015, **5**, 10699.
- 6 S. Sim, S. Li, W. Cai, B. Yu, X. Ju, J. Cao, Z. Dong, X. Yin, S. Shin, Y. Luo, D. Chi, A. Suwardi, H. K. Ng and J. Wu, *Advanced Science*, 2025, **12**, e09170.
- 7 S. H. Mir, V. K. Yadav and J. K. Singh, *ACS Omega*, 2020, **5**, 14203–14211.
- 8 O. Durante, K. Intonti, L. Viscardi, S. De Stefano, E. Faella, A. Kumar, A. Pelella, F. Romeo, F. Giubileo, M. S. G. Alghamdi, M. A. S. Alshehri, M. F. Craciun, S. Russo and A. Di Bartolomeo, *ACS Appl. Nano Mater.*, 2023, **6**, 21663–21670.
- 9 K. Intonti, A. Mazzotti, A. Pelella, F. Giubileo, N. Martucciello, S. O'Sullivan, V. Patil, P. K. Hurley, L. Ansari, F. Gity and A. Di Bartolomeo, *Mater. Horiz.*, 2026, 10.1039.D5MH01871D.
- 10 T. Knobloch, S. Selberherr and T. Grasser, *Nanomaterials*, 2022, **12**, 3548.
- 11 Y. Wang, Z. Pan, T. Zhou, X. Li, C. Luo, T. Zheng, W. Gao, Y. Zhang, Y. Yang, J. Li and N. Huo, *Materials Science and Engineering: R: Reports*, 2025, **165**, 101020.
- 12 Y. Zhang, S. Hu, Y. Zhou, T. Xu, Y. Peng, H. Deng, X. Bao and X. Zeng, *J. Electron. Mater.*, 2023, **52**, 5218–5226.
- 13 A. Mazzotti, K. Intonti, L. Viscardi, O. Durante, A. Spuri, A. Di Bernardo and A. Di Bartolomeo, in *2025 IEEE 25th International Conference on Nanotechnology (NANO)*, IEEE, Washington, DC, USA, 2025, pp. 255–260.



- 14 T. D. Ngo, Z. Yang, M. Lee, F. Ali, I. Moon, D. G. Kim, T. Taniguchi, K. Watanabe, K. Lee and W. J. Yoo, *Adv Elect Materials*, 2021, **7**, 2001212. View Article Online
DOI: 10.1039/D1TC00385K
- 15 C. D. Ornelas, A. Bowman, T. S. Walmsley, T. Wang, K. Andrews, Z. Zhou and Y.-Q. Xu, *ACS Appl. Mater. Interfaces*, 2020, **12**, 46476–46482.
- 16 J. Ding, X. Wang, Z. Song, S. Wang, Y. Lu, W. Wang, T. Han, F. Li, X. Zhu, L. Shan and M. Long, *Advanced Sensor Research*, 2023, **2**, 2300029.
- 17 A. Pelella, A. Kumar, K. Intonti, O. Durante, S. De Stefano, X. Han, Z. Li, Y. Guo, F. Giubileo, L. Camilli, M. Passacantando, A. Zak and A. Di Bartolomeo, *Small*, 2024, **20**, 2403965.
- 18 J.-K. Ko, I.-H. Park, K. Hong and K. C. Kwon, *Nanomaterials*, 2024, **14**, 1397.
- 19 A. Mirzaei, M. Alizadeh, H. R. Ansari, M. Moayedi, Z. Kordrostami, H. Safaeian, M. H. Lee, T. Kim, J. Kim, H. W. Kim and S. S. Kim, *Nanotechnology*, 2024, **35**, 332002.
- 20 A. Kumar, K. Intonti, L. Viscardi, O. Durante, A. Pelella, O. Kharsah, S. Sleziona, F. Giubileo, N. Martucciello, P. Ciambelli, M. Schleberger and A. Di Bartolomeo, *Mater. Horiz.*, 2024, **11**, 2397–2405.
- 21 M. H. Pervez, E. Elahi, M. A. Khan, M. Nasim, M. Asim, A. Rehmat, M. A. Rehman, M. A. Assiri, S. Rehman, J. Eom and M. F. Khan, *Small Structures*, 2025, **6**, 2400386.
- 22 S. De Stefano, O. Durante, A. Sessa, A. Politano, G. D'Olimpio, T. Dadiani, E. Faella, A. Dinescu, C. Parvulescu, C. Hetherington, C.-N. Kuo, C. S. Lue, M. Aldrigo, M. Passacantando and A. Di Bartolomeo, *ACS Appl. Mater. Interfaces*, 2025, **17**, 50901–50915.
- 23 J. Sung, S. W. Kim, D. Lee, S. Moon, E. Lee and H. H. Kim, *Small*, 2025, **21**, 2504024.
- 24 L. Viscardi, A. Mazzotti, O. Durante, T. Pucher, N. Martucciello, A. Castellanos-Gomez and A. Di Bartolomeo, *J. Phys. D: Appl. Phys.*, 2025, **58**, 265102.
- 25 P. Saha, M. Sahad E, S. Sathyanarayana and B. C. Das, *ACS Nano*, 2024, **18**, 1137–1148.
- 26 N. Krishnan K, S. Sathyanarayana and B. C. Das, *J. Mater. Chem. C*, 2024, **12**, 13827–13839.
- 27 M. K. Ghimire, H. Ji, H. Z. Gul, H. Yi, J. Jiang and S. C. Lim, *ACS Appl. Mater. Interfaces*, 2019, **11**, 10068–10073.
- 28 A. Sessa, S. De Stefano, O. Durante, A. Pelella, M. Aldrigo, C. Parvulescu, A. Dinescu, C. Kuo, C. S. Lue, T. Dadiani, G. D'Olimpio, E. Faella, A. Politano, M. Passacantando and A. Di Bartolomeo, *Adv Elect Materials*, 2026, e00734.
- 29 Q. H. Wang, K. Kalantar-Zadeh, A. Kis, J. N. Coleman and M. S. Strano, *Nature Nanotech*, 2012, **7**, 699–712.
- 30 D. P. Gulo, N. T. Hung, R. Sankar, R. Saito and H.-L. Liu, *Phys. Rev. Materials*, 2023, **7**, 044001.
- 31 Y. Pan, L. Zhu, L. Lu, J. Ou, J. Zhou, C. An and M. Dong, *Adv Funct Materials*, 2024, **34**, 2407931.
- 32 J. Wu, D. Luo, P. Wen, X. Han, C. Wang, H. Yu, W. Gao, X. Liu, G. Konstantatos, J. Li and N. Huo, *Advanced Optical Materials*, 2022, **10**, 2201902.
- 33 R. Ma, H. Zhang, Y. Yoo, Z. P. Degregorio, L. Jin, P. Golani, J. Ghasemi Azadani, T. Low, J. E. Johns, L. A. Bendersky, A. V. Davydov and S. J. Koester, *ACS Nano*, 2019, **13**, 8035–8046.
- 34 X. Hu, F. Zhang, Z. Hu, P. He, L. Tao, Z. Zheng, Y. Zhao, Y. Yang and J. He, *Optical Materials*, 2023, **136**, 113467.
- 35 S. S. Awate, K. Xu, J. Liang, B. Katz, R. Muzzio, V. H. Crespi, J. Katoch and S. K. Fullerton-Shirey, *ACS Nano*, 2023, **17**, 22388–22398.
- 36 H. Kowalczyk, J. Biscaras, N. Pistawala, L. Harnagea, S. Singh and A. Shukla, *ACS Nano*, 2023, **17**, 6708–6718.
- 37 Y. Tan, F. Luo, M. Zhu, X. Xu, Y. Ye, B. Li, G. Wang, W. Luo, X. Zheng, N. Wu, Y. Yu, S. Qin and X.-A. Zhang, *Nanoscale*, 2018, **10**, 19964–19971.
- 38 S. Yang, X. Xu, W. Xu, B. Han, Z. Ding, P. Gu, P. Gao and Y. Ye, *ACS Appl. Nano Mater.*, 2020, **3**, 10411–10417.
- 39 Y. Jeong, B. Han, A. Tamayo, N. Claes, S. Bals and P. Samori, *ACS Nano*, 2024, **18**, 18334–18343.



- 40 K. Intonti, A. Sessa, H. Neill, V. Patil, A. Pelella, N. Martucciello, L. Ansari, P. K. Hurley, F. Gity and A. Di Bartolomeo, in *2025 IEEE 25th International Conference on Nanotechnology (NANO)*, IEEE, Washington, DC, USA, 2025, pp. 588–593.
- 41 Y. Lin, Y. Xu, S. Wang, S. Li, M. Yamamoto, A. Aparecido-Ferreira, W. Li, H. Sun, S. Nakaharai, W. Jian, K. Ueno and K. Tsukagoshi, *Advanced Materials*, 2014, **26**, 3263–3269.
- 42 V. Patil, H. Neill, B. Sheehan, P. K. Hurley, L. Ansari and F. Gity, *Adv Elect Materials*, 2025, **11**, e00305.
- 43 G. Stan, C. V. Ciobanu, S. R. J. Likith, A. Rani, S. Zhang, C. A. Hacker, S. Krylyuk and A. V. Davydov, *ACS Appl. Mater. Interfaces*, 2020, **12**, 18182–18193.
- 44 O. F. N. Okello, D.-H. Yang, S.-Y. Seo, J. Park, G. Moon, D. Shin, Y.-S. Chu, S. Yang, T. Mizoguchi, M.-H. Jo and S.-Y. Choi, *ACS Nano*, 2024, **18**, 6927–6935.
- 45 W. Luo, M. Zhu, G. Peng, X. Zheng, F. Miao, S. Bai, X. Zhang and S. Qin, *Adv Funct Materials*, 2018, **28**, 1704539.
- 46 S. Larentis, B. Fallahzad, H. C. P. Movva, K. Kim, A. Rai, T. Taniguchi, K. Watanabe, S. K. Banerjee and E. Tutuc, *ACS Nano*, 2017, **11**, 4832–4839.
- 47 B. Yu, W. Kim, J. Jang, J. Lee, J. P. Hong, N. Kwon, S. Kim, A. Ha, H. Kim, J. Ahn, K. Jeong, T. Taniguchi, K. Watanabe, G. Wang, J. Ahn, S. Park and D. K. Hwang, *Adv Funct Materials*, 2024, **34**, 2404129.
- 48 G. Y. Bae, J. Kim, J. Kim, S. Lee and E. Lee, *Nanomaterials*, 2021, **11**, 2805.
- 49 Q. Wang, J. Chen, Y. Zhang, L. Hu, R. Liu, C. Cong and Z.-J. Qiu, *Nanomaterials*, 2019, **9**, 756.
- 50 J.-H. Li, D. Bing, Z.-T. Wu, G.-Q. Wu, J. Bai, R.-X. Du and Z.-Q. Qi, *Chinese Phys. B*, 2020, **29**, 017802.
- 51 M. Yamamoto, S. T. Wang, M. Ni, Y.-F. Lin, S.-L. Li, S. Aikawa, W.-B. Jian, K. Ueno, K. Wakabayashi and K. Tsukagoshi, *ACS Nano*, 2014, **8**, 3895–3903.
- 52 X. Luo, Y. Zhao, J. Zhang, M. Toh, C. Kloc, Q. Xiong and S. Y. Quek, *Phys. Rev. B*, 2013, **88**, 195313.
- 53 C. Ruppert, B. Aslan and T. F. Heinz, *Nano Lett.*, 2014, **14**, 6231–6236.
- 54 H. Li, Q. Zhang, C. C. R. Yap, B. K. Tay, T. H. T. Edwin, A. Olivier and D. Baillargeat, *Adv Funct Materials*, 2012, **22**, 1385–1390.
- 55 W. Zhao, Z. Ghorannevis, K. K. Amara, J. R. Pang, M. Toh, X. Zhang, C. Kloc, P. H. Tan and G. Eda, *Nanoscale*, 2013, **5**, 9677.
- 56 S. Smidstrup, T. Markussen, P. Vancraeyveld, J. Wellendorff, J. Schneider, T. Gunst, B. Verstichel, D. Stradi, P. A. Khomyakov, U. G. Vej-Hansen, M.-E. Lee, S. T. Chill, F. Rasmussen, G. Penazzi, F. Corsetti, A. Ojanperä, K. Jensen, M. L. N. Palsgaard, U. Martinez, A. Blom, M. Brandbyge and K. Stokbro, *J. Phys.: Condens. Matter*, 2020, **32**, 015901.
- 57 M. J. Van Setten, M. Giantomassi, E. Bousquet, M. J. Verstraete, D. R. Hamann, X. Gonze and G.-M. Rignanese, *Computer Physics Communications*, 2018, **226**, 39–54.
- 58 H. J. Monkhorst and J. D. Pack, *Phys. Rev. B*, 1976, **13**, 5188–5192.
- 59 S. Grimme, J. Antony, S. Ehrlich and H. Krieg, *The Journal of Chemical Physics*, 2010, **132**, 154104.
- 60 J. Heyd, G. E. Scuseria and M. Ernzerhof, *The Journal of Chemical Physics*, 2003, **118**, 8207–8215.
- 61 V. Patil, H. Neill, B. Sheehan, P. K. Hurley, L. Ansari and F. Gity, *Adv Elect Materials*, 2025, **11**, e00305.
- 62 S. Kim, J. H. Kim, D. Kim, G. Hwang, J. Baik, H. Yang and S. Cho, *2D Mater.*, 2017, **4**, 024004.
- 63 G. Makov and M. C. Payne, *Phys. Rev. B*, 1995, **51**, 4014–4022.
- 64 T. Kim, D. Joung and J. Park, *Current Applied Physics*, 2018, **18**, 843–846.
- 65 S. M. Sze and K. K. Ng, *Physics of Semiconductor Devices*, Wiley, 1st edn., 2006.



- 66 W. Li, E. Chen, D. Li, Z. Lu, X. Zheng, X. Wang, X. Wan and K. Chen, *Adv Materials Technologies*, 2025, **10**, 70024. View Article Online
DOI: 10.1039/D6TC00385K
- 67 A. Grillo and A. Di Bartolomeo, *Adv Elect Materials*, 2021, **7**, 2000979.
- 68 A. Di Bartolomeo, A. Grillo, F. Urban, L. Iemmo, F. Giubileo, G. Luongo, G. Amato, L. Croin, L. Sun, S. Liang and L. K. Ang, *Adv Funct Materials*, 2018, **28**, 1800657.
- 69 A. Di Bartolomeo, K. Intonti, L. Peluso, R. Di Marco, G. Vocca, F. Romeo, F. Giubileo, A. Grillo and E. Orhan, *Nano Ex.*, 2025, **6**, 022501.
- 70 A. Sessa, T. Dadiani, S. De Stefano, O. Durante, A. Pelella, C. Parvulescu, A. Dinescu, M. Aldrigo, C. Kuo, C. S. Lue, G. D'Olimpio, E. Faella, A. Politano, M. Passacantando and A. Di Bartolomeo, *Adv Elect Materials*, 2025, **11**, e00327.
- 71 S. Bitter, P. Schlupp, H. Von Wenckstern and M. Grundmann, *ACS Appl. Mater. Interfaces*, 2017, **9**, 26574–26581.
- 72 A. Di Bartolomeo, L. Genovese, F. Giubileo, L. Iemmo, G. Luongo, T. Foller and M. Schleberger, *2D Mater.*, 2017, **5**, 015014.
- 73 S. Abedin, V. Kurtash, S. Mathew, S. Thiele, H. O. Jacobs and J. Pezoldt, *Materials*, 2024, **17**, 1350.
- 74 A. K. Rai, A. A. Shah, J. Kumar, S. Chattaraj, A. B. Dar, U. Patbhaje and M. Shrivastava, *ACS Nano*, 2024, **18**, 6215–6228.
- 75 M. W. Iqbal, E. Elahi, A. Amin, S. Aftab, I. Aslam, G. Hussain and M. A. Shehzad, *Superlattices and Microstructures*, 2020, **147**, 106698.
- 76 D. Qu, X. Liu, M. Huang, C. Lee, F. Ahmed, H. Kim, R. S. Ruoff, J. Hone and W. J. Yoo, *Advanced Materials*, 2017, **29**, 1606433.
- 77 F. Giannazzo, G. Fisichella, A. Piazza, S. Di Franco, G. Greco, S. Agnello and F. Roccaforte, *Beilstein J. Nanotechnol.*, 2017, **8**, 254–263.
- 78 A. Di Bartolomeo, L. Genovese, F. Giubileo, L. Iemmo, G. Luongo, T. Foller and M. Schleberger, *2D Mater.*, 2017, **5**, 015014.
- 79 D. J. Late, B. Liu, H. S. S. R. Matte, V. P. Dravid and C. N. R. Rao, *ACS Nano*, 2012, **6**, 5635–5641.
- 80 F. Ahmed, A. M. Shafi, D. M. A. Mackenzie, M. A. Qureshi, H. A. Fernandez, H. H. Yoon, M. G. Uddin, M. Kuittinen, Z. Sun and H. Lipsanen, *Adv Materials Inter*, 2021, **8**, 2100950.
- 81 A. Rani, K. DiCamillo, M. A. H. Khan, M. Paranjape and M. E. Zaghloul, *Sensors*, 2019, **19**, 2551.
- 82 S. Nisar, M. Shahzadi, Z. M. Shahzad, D. Kim, G. Dastgeer and A. Irfan, *ACS Appl. Electron. Mater.*, 2023, **5**, 5714–5721.
- 83 S. Fathipour, N. Ma, W. S. Hwang, V. Protasenko, S. Vishwanath, H. G. Xing, H. Xu, D. Jena, J. Appenzeller and A. Seabaugh, *Applied Physics Letters*, 2014, **105**, 192101.
- 84 M. Zhang, J. Li, K. Shi, X. Fang, Y. Zhai, G. Qu, W. Wang and Z. Jiang, *Materials Research Bulletin*, 2025, **185**, 113275.
- 85 Y. Jeong, B. Han, A. Tamayo, N. Claes, S. Bals and P. Samorì, *ACS Nano*, 2024, **18**, 18334–18343.
- 86 Y. Kim, A. Venkatesan, J. Kim, H. Kim, K. Watanabe, T. Taniguchi, D. Whang and G.-H. Kim, *Materials Science in Semiconductor Processing*, 2023, **153**, 107133.
- 87 W. Huang, Y. Zhang, M. Song, B. Wang, H. Hou, X. Hu, X. Chen and T. Zhai, *Chinese Chemical Letters*, 2022, **33**, 2281–2290.
- 88 Y. Park, H. W. Baac, J. Heo and G. Yoo, *Applied Physics Letters*, 2016, **108**, 083102.
- 89 H. Jawa, A. Varghese and S. Lodha, *ACS Appl. Mater. Interfaces*, 2021, **13**, 9186–9194.
- 90 A. Di Bartolomeo, A. Pelella, X. Liu, F. Miao, M. Passacantando, F. Giubileo, A. Grillo, L. Iemmo, F. Urban and S. Liang, *Adv Funct Materials*, 2019, **29**, 1902483.
- 91 A. Mazzotti, O. Durante, S. De Stefano, L. Viscardi, A. Pelella, O. Kharsah, L. Daniel, S. Sleziona, M. Schleberger and A. Di Bartolomeo, *Advanced Optical Materials*, 2025, **13**, 2500811.



- 92 R. T. Tung, *Phys. Rev. B*, 1992, **45**, 13509–13523.
- 93 A. S. Kavasoglu, C. Tozlu, O. Pakma, N. Kavasoglu, S. Ozden, B. Metin, O. Birgi and S. Oktik, *J. Phys. D: Appl. Phys.*, 2009, **42**, 145111.
- 94 Ş. Aydoğan, M. Sağlam, A. Türüt and Y. Onganer, *Synthetic Metals*, 2005, **150**, 15–20.
- 95 J. H. Werner and H. H. Güttler, *Journal of Applied Physics*, 1991, **69**, 1522–1533.
- 96 R. T. Tung, *Materials Science and Engineering: R: Reports*, 2001, **35**, 1–138.
- 97 J. Tersoff, *Phys. Rev. Lett.*, 1984, **52**, 465–468.
- 98 J. Bardeen, in *Electronic Structure of Metal-Semiconductor Contacts*, ed. W. Mönch, Springer Netherlands, Dordrecht, 1999, vol. 4, pp. 63–73.
- 99 K. K. Chin, R. Cao, T. Kendelewicz, K. Miyano, M. D. Williams, S. Doniach, I. Lindau and W. E. Spicer, *MRS Proc.*, 1986, **77**, 297.
- 100 X. Liu, M. S. Choi, E. Hwang, W. J. Yoo and J. Sun, *Advanced Materials*, 2022, **34**, 2108425.
- 101 C. Kim, I. Moon, D. Lee, M. S. Choi, F. Ahmed, S. Nam, Y. Cho, H.-J. Shin, S. Park and W. J. Yoo, *ACS Nano*, 2017, **11**, 1588–1596.
- 102 J. Xie, N. M. Patoary, G. Zhou, M. Y. Sayyad, S. Tongay and I. S. Esqueda, *Nanotechnology*, 2022, **33**, 225702.
- 103 N. Huo, Y. Yang, Y.-N. Wu, X.-G. Zhang, S. T. Pantelides and G. Konstantatos, *Nanoscale*, 2018, **10**, 15071–15077.
- 104 K. S. Bhargavi and S. S. Kubakaddi, *J. Phys.: Condens. Matter*, 2014, **26**, 485013.
- 105 A. Pelella, V. Demontis, A. Sessa, A. Mazzotti, F. Giubileo, V. Zannier, L. Sorba, F. Rossella and A. Di Bartolomeo, *Adv Elect Mater*, 2025, **11**, e00520.
- 106 N. S. Ndiaye, O. Simonetti, T.-P. Nguyen and L. Giraudet, *Organic Electronics*, 2021, **99**, 106350.
- 107 Y. Shao, J. Yoon, H. Kim, T. Lee and W. Lu, *Applied Surface Science*, 2014, **301**, 2–8.
- 108 G. Kim, D. X. Dang, H. Z. Gul, H. Ji, E. K. Kim and S. C. Lim, *Nanotechnology*, 2024, **35**, 035702.
- 109 H. Ji, G. Lee, M.-K. Joo, Y. Yun, H. Yi, J.-H. Park, D. Suh and S. C. Lim, *Applied Physics Letters*, 2017, **110**, 183501.
- 110 V. O. Khaustov, J. Köster, M. W. Ochapski, A. A. Zakharov, D. Convertino, Z. M. Gebeyehu, L. Martini, N. Mishra, G. Marini, M. Calandra, U. Kaiser, S. Forti and C. Coletti, *2D Mater.*, 2025, **12**, 025025.
- 111 H. Ryu, Y. Lee, J. H. Jeong, Y. Lee, Y. Cheon, K. Watanabe, T. Taniguchi, K. Kim, H. Cheong, C. Lee and G. Lee, *Small*, 2023, **19**, 2205224.
- 112 C. Wang, X. Liu, X. Li, Z. Yao, W. Hong and T. Jiao, *ACS Materials Lett.*, 2026, **8**, 76–98.
- 113 B. S. Y. Kim, T. D. Ngo, Y. Hassan, S. H. Chae, S. Yoon and M. S. Choi, *Advanced Science*, 2024, **11**, 2407175.
- 114 B. Sirota, N. Glavin, S. Krylyuk, A. V. Davydov and A. A. Voevodin, *Sci Rep*, 2018, **8**, 8668.



Data availability statement

View Article Online
DOI: 10.1039/D6TC00385K

The data supporting the findings of this study are available from the corresponding authors upon reasonable request.

